Engineering Structures 281 (2023) 115736

Contents lists available at ScienceDirect

Engineering Structures

journal homepage: www.elsevier.com/locate/engstruct

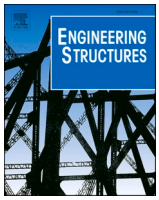

Experimental study of DED-arc additively manufactured steel double-lap shear bolted connections

Xi Guo [a,*], Pinelopi Kyvelou [a], Jun Ye [a], Lip H. Teh [b], Leroy Gardner [a]

[a] Department of Civil and Environmental Engineering, Imperial College London, London SW7 2AZ, UK
[b] School of Civil, Mining and Environmental Engineering, University of Wollongong, Wollongong 2500, Australia

ARTICLE INFO

Keywords:
3D printing
Bolted connections
End-splitting
Localised tearing
Shear-out
Incidental block shear
Double-shear connections
Wire arc additive manufacturing

ABSTRACT

An experimental study into the structural behaviour of Directed Energy Deposition-arc or wire arc additively manufactured (DED-arc AM and WAAM, respectively) steel double-lap shear bolted connections is presented. The mechanical properties of the material, which had a nominal yield stress of 420 MPa, were first determined by means of tensile coupon tests. Sixty connection specimens of two different nominal thicknesses and two print layer orientations were then tested to failure. The geometry of the test specimens was determined by 3D laser scanning, while the deformation and strain fields were measured during testing using digital image correlation. The observed failure modes included shear-out, net section tension, bearing and end-splitting, while a new hybrid mode of shear-out and net section tension was identified for the first time. The test results were compared against the predictions of current design specifications, namely AISI S100 and AS/NZS 4600 for cold-formed steel and AISC 360 and Eurocode 3 for structural steel, to evaluate their applicability to WAAM elements. Overall, the structural behaviour of the tested specimens followed the anticipated trends, and the predicted resistances determined from the current design specifications were generally reasonable. There were, however, a number of exceptions to this, highlighting the need for new design provisions, together with appropriate safety factors, that are specific to this form of manufacture.

1. Introduction

Directed Energy Deposition-arc (DED-arc) additive manufacturing (AM), also known as wire arc additive manufacturing (WAAM) is a method of 3D printing that can be used for the fabrication of large-scale structural elements. WAAM offers geometric freedom, good structural integrity, reasonable build times, enhanced automation and scope for substantial material saving through optimisation [1–7]. The potential impact of WAAM on the construction sector, both in terms of efficiency and reduction in environmental footprint, is therefore very significant. A deeper understanding, further experimental data and reliable design rules are however needed before wider application of this novel technology can take place.

Bolted connections feature in most structural steel joints due to their low cost and ease of assembly. Their structural behaviour has therefore been extensively investigated [8–19], including a number of studies into the influence of their geometric characteristics [20–23], material types [24–29], bolt preload and loading direction [30–32] on their load-deformation response. Winter [33] identified four distinct failure modes for bolted connections, namely shear-out failure, net section tension failure, bearing failure and bolt shearing failure – see Fig. 1. In addition to the aforementioned failure modes, other types of failure have also since been identified. Localised-tearing failure was first observed in [34], with its occurrence linked to curling and localised bearing stresses developing at the edge of the bolt hole, with fracture extending diagonally, while tilt-bearing failure, defined as the bolt head or nut punching through the plate on the upstream side, was identified in [35]. More recently, curl-bearing failure, characterised by the bolt head penetrating into the lap plate downstream of the bolt hole due to significant curling, was identified for the first time in [36], where it was also shown that the ultimate capacities corresponding to curl-bearing and localised-tearing failures can be predicted by the equation [35] originally developed for tilt-bearing failure.

In this paper, a total of sixty double-lap shear tests on WAAM bolted connections is presented. The production, measurement and testing of the specimens are described while the test results are analysed and the observed failure modes are discussed. Finally, comparisons are made against the capacity predictions yielded by current design standards.

* Corresponding author.
E-mail address: x.guo19@imperial.ac.uk (X. Guo).

https://doi.org/10.1016/j.engstruct.2023.115736
Received 18 August 2022; Received in revised form 23 January 2023; Accepted 29 January 2023
Available online 18 February 2023

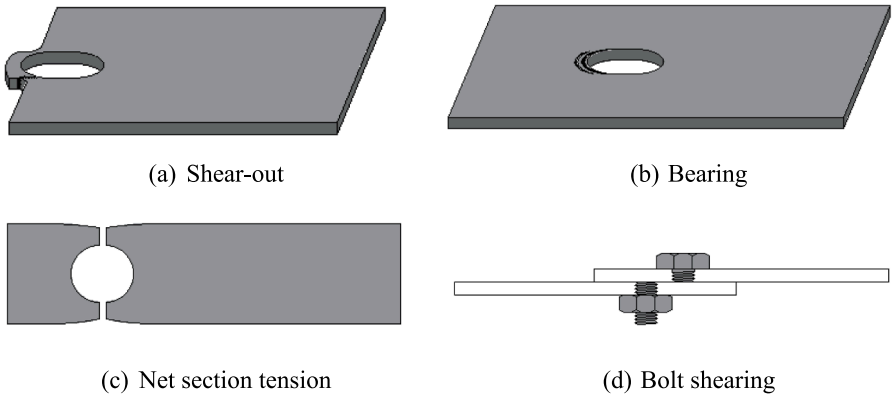

Fig. 1. Failure modes of bolt connections.

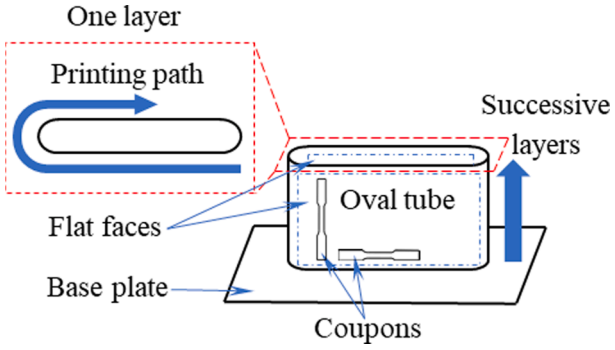

Fig. 2. Printing process.

2. Manufacturing and geometric measurements of test specimens

All specimens were extracted by means of waterjet cutting from flat-sided oval tubes (adopted for their ease of continuous printing and geometric stability during production), which were fabricated by MX3D [37] using multi-axis robotic WAAM technology; the printing process is illustrated in Fig. 2. The feedstock material was welding wire ER70S-6 (EN ISO 14341-A G 42 3 M21 3Si1), where the letter G indicates gas-shielded metal arc welding, the number 42 denotes a minimum yield strength of 420 MPa, a tensile strength between 500 MPa and 640 MPa and a minimum elongation at fracture of 20%, the number 3 indicates that at a temperature of −30 °C a minimum average impact energy of 47 J is achieved, the notation M21 is the classification of the shielding gas, and the 3Si1 refers to the chemical composition of the wire electrode [36,38]. The chemical composition and mechanical properties, as provided by the manufacturer, are presented in Tables 1 and 2 respectively, with a carbon equivalent value (Pcm) of 0.17. The employed printing parameters are presented in Table 3, where the high welding current was adopted for the printing of the 8 mm components to efficiently increase the energy input, in order to realise the printing of the thicker material. Following their extraction from the parent plates (i.e. the flat sides of the oval tubes), the specimens were sandblasted with glass beads. Laser scanning of the undulating surfaces of the WAAM specimens was subsequently performed using a triangulation-based FARO Design ScanArm 2.0 laser scanner, capable of capturing 600,000 points per second with an accuracy of 0.075 mm [39]. A point cloud of each scanned specimen was then created by merging multiple scans in the software Geomagic Wrap [40], which was then inter-connected to form a polygon mesh and, finally, a 3D CAD model. A typical specimen along with its scanned point cloud and 3D CAD model is illustrated in Fig. 3, while a flow chart of the steps followed for the preparation of all specimens is illustrated in Fig. 4.

The key geometric parameters affecting the structural performance of bolted lap-shear connections are the width of the connected plate b, the bolt hole diameter d_0, the distance between the centre of the bolt hole and the end of the plate (termed the end distance) e_1 and the thickness of the plate t – see Fig. 5. The specimens examined herein were suitably proportioned to ensure the occurrence of three different failure modes, namely shear-out, net section tension and bearing.

For each set of dimensions, two specimens were fabricated but with different angles (i.e. 0° and 90°) between the print layer orientation and the loading direction, to investigate the possible influence of material anisotropy and the geometrical undulations inherent to the WAAM process – see Fig. 6. Sixty specimens were fabricated in total. The labelling system adopted for the test specimens starts with the letter D (for double-shear), followed by the nominal thickness t, nominal width b

Table 2
Mechanical properties (as welded) of feedstock wire [36].

Yield strength (MPa)	Ultimate tensile strength (MPa)	Elongation A5 (%)	Impact energy at 40 °C (J)
471	580	25	73

Table 3
Printing parameters for WAAM material of two nominal thicknesses t_{nom} [36].

Printing parameter	t_{nom}	
	3 mm	8 mm
Wire diameter (mm)	0.8	1.2
Travel speed (mm/s)	8	8
Wire feed speed (m/min)	3	4
Welding voltage (V)	14.8	24.8
Welding current (A)	54	130
Gas flow rate (L/min)	14	16
Shielding gas	80 % Ar + 20 % CO_2	
Welding mode	Short-arc	Pulsed
Dwell time (s)	30	30

Table 1
Chemical composition (% by weight) of feedstock wire [36].

C	Si	Mn	P	S	Cr	Ni	Mo	Cu	V	Ai	Zr + Ti
0.07	0.85	1.43	0.007	0.006	0.04	0.01	0.01	0.01	0.01	0.01	0.02

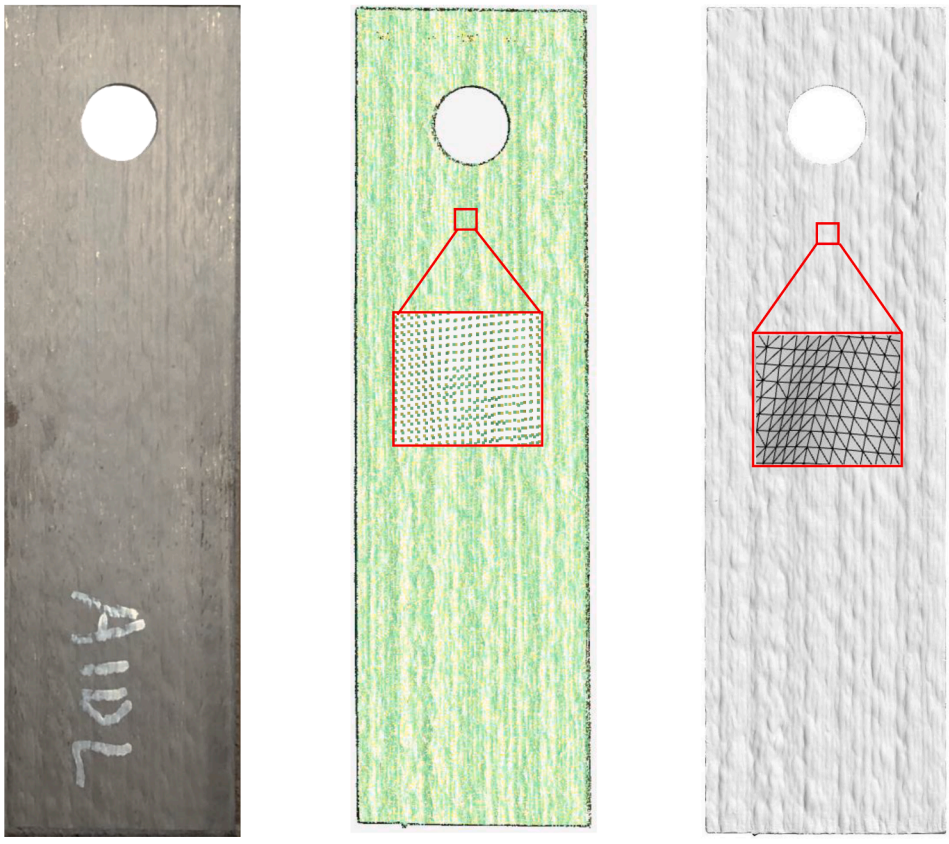

(a) Specimen after sandblasting

(b) Point cloud (50% of points displayed)

(c) 3D CAD model (STL file)

Fig. 3. Real specimen and digital models.

and nominal end distance e_1 in mm and, finally, by the number 0 or 90 to denote the angle between the print layer orientation and the loading direction (in degrees). For example, Specimen D3-55-27-90 is a double-shear lap specimen with a 3 mm nominal thickness, a 55 mm nominal width, a 27 mm nominal end distance and a 90° angle between the print layer orientation and the loading direction.

The width b, bolt hole diameter d_0 and end distance e_1 of all specimens were measured using Vernier callipers and are presented in Table 4. However, due to the inherent surface undulations of the as-built WAAM specimens, the magnitude of which are influenced by the quality of the printing, use of conventional means for thickness measurements was deemed to be inappropriate [41–43]; laser scanning was therefore employed. The 3D CAD models of all specimens obtained from the laser scans were imported into the software Rhino 3D [44] as STL files, where the average thicknesses t, reported in Table 4, were determined following the process described in [43]. Note that the specimen lengths were about three times their respective widths, varying from 190 mm to 390 mm.

3. Material tests

Tensile coupon tests, reported in detail in [36], were carried out in accordance with EN ISO 6892-1 [45] to determine the material stress-strain characteristics of the WAAM material. Material anisotropy was investigated by extracting coupons from WAAM plates at 0°, 45° and 90° to the print layer orientation (see Fig. 6).

The effective material properties determined from the tested coupons, namely the Young's modulus E, yield strength f_y (defined as the 0.2 % proof stress), ultimate tensile strength f_u, ultimate tensile strain ε_u and fracture strain ε_f (determined according to EN ISO 6892-1 [45]) are presented in Table 5, grouped by nominal thickness t_{nom}.

Slight material anisotropy was observed, with the differences in Young's modulus, yield strength and ultimate tensile strength between the two print layer directions being limited to 15% at most, while the yield strength and ultimate tensile strength of the thinner material were found to be higher than the respective values of the thicker material (by 23% and 17% respectively). Similar findings were reported in [46].

4. Double-lap shear lap tests

4.1. Test setup

All connection tests were carried out using a 600 kN Instron testing machine. Each WAAM plate was positioned between two grade S700 high-strength steel (HSS) plates, and connected using a fully threaded grade 12.9 bolt in a 2 mm clearance hole. The size of the bolts varied from M16 to M30, depending on the size of the connected plates and the estimated ultimate load, to avoid bolt shear failure. The bolts were finger-tightened to limit the influence of preloading and friction [30,31,47]. A digital image correlation (DIC) system comprising two pairs of cameras was employed, with each camera pair monitoring one side of the specimen during testing. Prior to the tests, the WAAM specimens, HSS plates and bolts were painted black and then sprayed with a white random speckle pattern, to create contrasting features that would be readily captured by the DIC system, enabling the effective tracking of displacements and strains. For the tests presented herein, the reported

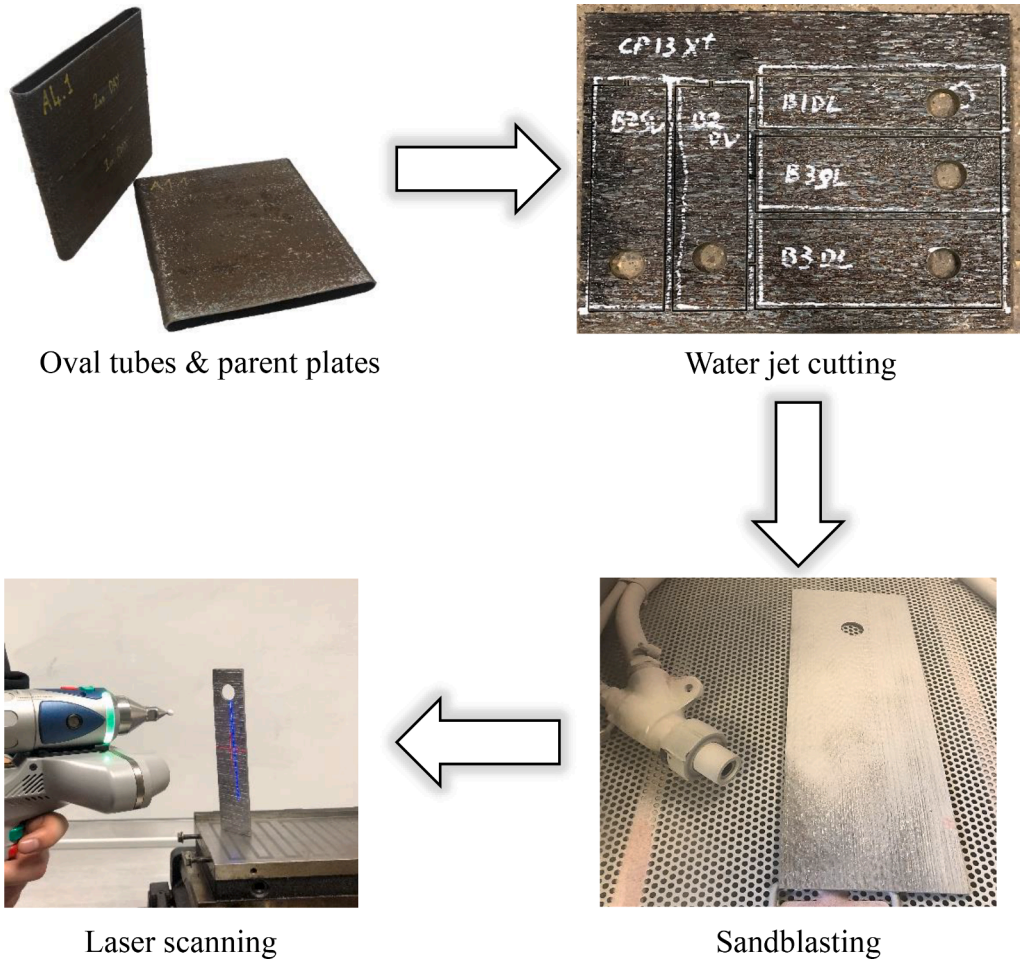

Fig. 4. Preparation process of typical specimen.

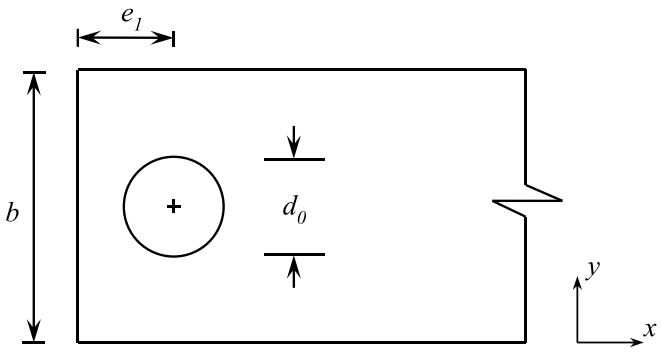

Fig. 5. Basic configuration of test specimens.

displacements of the test specimens extracted from the DIC system (see Section 4.3) were measured over a gauge length of about 150 mm. An overview of the test setup is presented in Fig. 7.

4.2. Failure modes

The failure modes observed for all tested specimens are presented in Table 6, where SO stands for shear-out, NS for net section tension, B for bearing and ES for end-splitting. Each failure mode is analysed and discussed in this section.

4.2.1. Shear-out, net section tension and bearing failures

The specimens that failed in shear-out were sized such that their end distance e_1 was short and their width b was relatively large, resulting in the material at the end of the WAAM plate being pulled out – see Fig. 8 (a). For specimens with narrower plate widths, significant necking was observed along the net section, eventually leading to net section tension fracture – see Fig. 8(b). For specimens with end distances and widths sufficiently large to avoid both shear-out and net section tension failures, the bolt bore into the WAAM plate, piling up the material downstream of the bolt hole and causing bearing failure. It is worth noting that for a failure mode to be classified as bearing, a significant amount of material piling up downstream of the bolt hole is a prerequisite, with no deformation at the end (parallel to the loading) prior to bearing fracture – see Fig. 8(c).

4.2.2. End-splitting failure

End-splitting is a failure mode characterised by fracture initiated at the free end of the plate, propagating in the loading direction, and is attributed to the development of high transverse tensile stresses (i.e. along the y axis as per Fig. 5). The earliest description of end-splitting failure was found by the authors in a test report on stainless steel bolted connections in 1976 [48], where the failure mechanism was described as a "splay", caused by the rotation of the net section, leading to the end of the plate spreading outwards. Since then, end-splitting failure has been observed by several researchers [17,21,32,49,50]. In [17], end-splitting failure was described as a transition between shear-out and net section tension failure, while in [21,49,50], end-spitting failure was defined as the lower boundary of the bearing resistance of

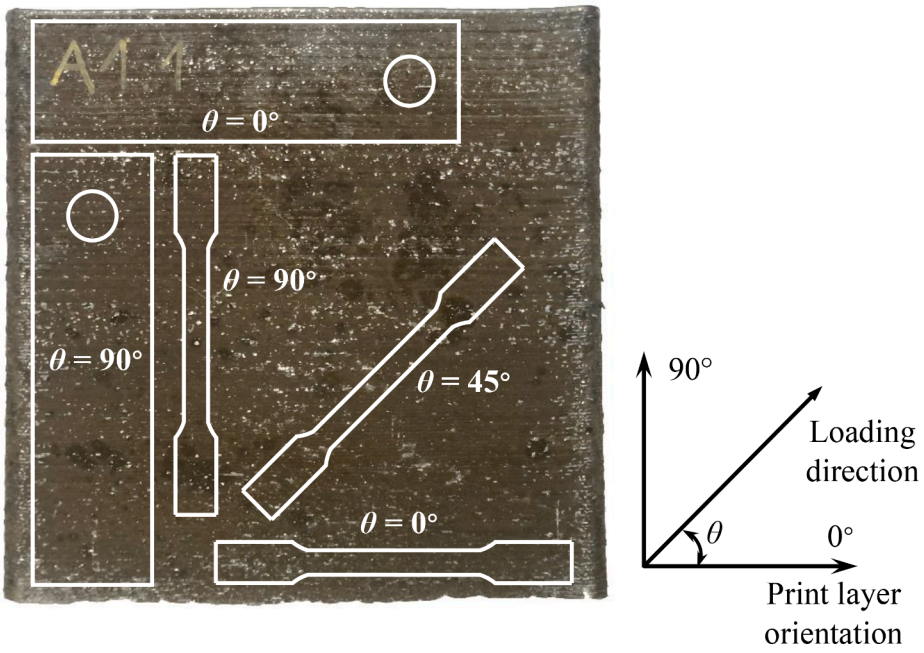

Fig. 6. Orientation of tensile coupons and lap specimens extracted from WAAM plates relative to print layer orientation [36].

a lap connection. In all incidents of the failure mode, plastic deformation and rotation of the net section have been observed; some researchers have found that the occurrence of end-splitting is related to the cutting and fabrication methods of the connected steel plates [18,32].

End-splitting failure was also exhibited by some of the specimens examined herein; typical examples are shown in Fig. 9, where specimens of the same width (i.e. $b = 65$ mm) and of increasing end distances e_1 (i.e. from 21.6 to 36 mm) are grouped by their angle θ relative to the print layer orientation (i.e. (a) $\theta = 0°$ and (b) $\theta = 90°$). Note that in the current investigation, a failure was identified as end-splitting if the visual occurrence of fracture at the end was accompanied by an abrupt drop in load. The specimens shown in Fig. 9(a) have the same dimensions as those shown in Fig. 9(b), but different print layer orientations.

All the $\theta = 0°$ specimens shown in Fig. 9(a) underwent end-splitting failure irrespective of the ratio e_1/b. Although it was stated in [49] that end-splitting fracture only occurs because of partial yielding in the net cross-section thus enabling rotation at this location as well as outward bending at the edge of the plate, which is consistent with the observation on Specimen D3-65-36-0, rotation at the net cross-section of Specimen D3-65-21.6-0 was barely evident. On the other hand, with increasing end distance, the failure mode of the $\theta = 90°$ specimens first transitioned from shear-out (Specimen D3-65-21.6-90) to end-splitting (Specimens D3-65-27-90 and D3-65-32.4-90) and then reverted back to shear-out (Specimen D3-65-36-90), indicating that the occurrence of end-splitting failure is more strongly related to the level of material imperfections at the plate end rather than the plate geometry. This indication is supported not only by the fact that all the $\theta = 0°$ specimens underwent end-splitting failure while only half of the $\theta = 90°$ specimens did, but also by the findings from previous studies that specimens with sheared ends were more prone to end-splitting than those with saw cut ends [18,32].

4.2.3. *Incidental block shear failure*

Figs. 10(a) and 10(b) show the "incidental" block shear failures of Specimens D3-65-43.2-90 and D3-65-43.2-0, respectively. An incidental block shear failure may occur in a single bolted connection when the net section tension capacity is nominally the same as the shear-out capacity. In this case, either a net section tension failure, a shear-out failure, or an incidental block shear may take place, depending on the weakest tensile and/or shear planes caused by fabrication or material imperfections. If the two weakest planes are the planes at the net tensile section, then net section tension fractures will govern. Shear-out will govern if the two shear planes are weaker than the two tensile planes on either side of the bolt. If the two weakest planes comprise a shear plane and a tensile plane on the other side of the bolt (in order to maintain equilibrium), then the member will undergo an incidental block shear failure.

End-splitting failure was observed only for Specimen D3-65-43.2-0, further verifying that this mode of failure is strongly linked to the local conditions at the plate end and, in the context of WAAM connections, is dependent on the print layer orientation rather than the plate geometry.

4.3. *Ultimate loads and load-deformation responses*

The ultimate loads P_u of all test specimens are reported in Table 6, while the load-displacement curves are presented in Fig. 11, where the displacements were calculated as the average of the measurements from both sides of the specimens, over a gauge length of about 150 mm – see Fig. 7. Note that some curves in Figs. 11(c) and 11(d), corresponding to the specimens failing in bearing are not as smooth as the others. The temporary reductions in stiffness are attributed to the local buckling of the region downstream of the bolt. Meanwhile, the sharp drops and subsequent recoveries in the curves are attributed to the irregular fracture paths of the WAAM plates with very long end distances. Localised fractures developed well before the ultimate bearing failure load, but could not propagate further even with an increase in the applied load since the load (or stress) direction was not sympathetic to the fracture direction. As the bearing deformation proceeded, one or more localised fractures could also ensue at higher loads until the ultimate bearing failure. Typical load-displacement curves of specimens failing in shear-out, net section tension, bearing and splitting are presented in Fig. 12.

The load-displacement curve of Specimen D3-65-21.6-0 is presented in Fig. 13, where the curve of Specimen D3-65-21.6-90, which failed in shear-out, is also plotted. Unlike the smooth curve of Specimen D3-65-21.6-90, a rather sudden change in gradient can be noticed at the ultimate load point, indicating the occurrence of fracture. Thus, it can be concluded that Specimen D3-65-21.6-0 failed by end-splitting.

Table 4
Measured geometric properties of test specimens.

Specimen	Bolt type	t (mm)	d_0 (mm)	b (mm)	e_1 (mm)
D3-35-27-0	M16	2.7	18.4	34.7	26.6
D3-45-27-0	M16	2.9	17.8	45.3	27.2
D3-45-36-0	M16	2.9	17.9	45.5	36.2
D3-55-27-0	M16	2.6	18.1	55.2	27.1
D3-65-21.6-0	M16	2.8	17.8	65.4	21.7
D3-65-27-0	M16	2.9	17.9	65.4	27.2
D3-65-32.4-0	M16	2.9	17.8	65.4	32.5
D3-65-36-0	M16	2.8	17.8	65.4	36.0
D3-65-43.2-0	M16	2.8	17.8	65.4	43.5
D3-85-33-0	M20	2.8	21.8	85.4	33.2
D3-85-57.2-0	M20	2.8	21.9	85.5	57.5
D3-105-37.4-0	M20	2.6	22.6	104.8	38.7
D3-105-39.6-0	M20	2.7	22.8	104.5	37.3
D3-105-48.4-0	M20	2.7	22.4	104.4	47.9
D3-145-91-0	M24	2.7	26.1	144.2	90.5
D3-145-104-0	M24	2.7	26.0	142.6	103.3
D3-145-117-0	M24	2.7	26.3	124.0	115.7
D8-45-44.2-0	M24	7.8	26.2	44.9	43.9
D8-55-44.2-0	M24	7.9	26.0	54.9	44.1
D8-75-44.2-0	M24	7.2	26.2	74.9	44.5
D8-80-44.2-0	M24	7.9	25.9	79.9	44.1
D8-90-26-0	M24	7.7	25.8	90.2	25.9
D8-90-39-0	M24	7.7	26.0	90.2	39.0
D8-90-52-0	M24	7.5	25.9	90.2	52.0
D8-90-65-0	M24	7.5	25.9	90.1	65.2
D8-90-91-0	M24	7.6	25.9	90.3	91.3
D8-120-48-0	M30	7.4	31.8	120.1	48.0
D8-120-64-0	M30	7.5	31.8	120.1	64.1
D8-120-80-0	M30	7.5	32.0	120.0	80.0
D8-120-112-0	M30	7.5	32.0	120.0	111.7
D3-35-27-90	M16	2.7	18.0	35.2	27.0
D3-45-27-90	M16	2.9	17.8	45.2	27.3
D3-45-36-90	M16	3.0	17.7	45.4	36.2
D3-55-27-90	M16	2.7	18.2	55.3	27.1
D3-65-21.6-90	M16	2.9	17.8	65.3	21.7
D3-65-27-90	M16	2.9	17.9	65.2	27.2
D3-65-32.4-90	M16	2.9	17.9	65.3	32.6
D3-65-36-90	M16	2.8	17.9	65.6	36.5
D3-65-43.2-90	M16	2.7	17.9	65.3	43.7
D3-85-33-90	M20	2.7	21.9	85.3	33.1
D3-85-57.2-90	M20	2.8	21.9	85.5	57.3
D3-105-37.4-90	M20	2.8	22.1	105.0	37.4
D3-105-39.6-90	M20	2.8	22.2	105.3	39.5
D3-105-48.4-90	M20	2.8	22.2	104.9	48.2
D3-145-91-90	M24	2.7	25.8	143.8	91.0
D3-145-104-90	M24	2.6	26.1	144.3	104.1
D3-145-117-90	M24	2.7	26.4	143.7	118.4
D8-45-44.2-90	M24	7.4	26.0	44.7	43.9
D8-55-44.2-90	M24	7.4	26.2	54.7	43.9
D8-75-44.2-90	M24	7.4	26.0	74.8	44.1
D8-80-44.2-90	M24	7.4	26.2	79.9	44.3
D8-90-26-90	M24	7.7	25.9	90.2	26.0
D8-90-39-90	M24	7.6	25.9	90.3	39.1
D8-90-52-90	M24	7.6	25.9	90.1	52.3
D8-90-65-90	M24	7.7	25.7	90.2	65.0
D8-90-91-90	M24	7.6	25.9	90.2	91.1
D8-120-48-90	M30	7.6	31.8	120.3	48.0
D8-120-64-90	M30	7.6	31.8	120.2	64.0
D8-120-80-90	M30	7.8	31.9	120.1	80.1
D8-120-112-90	M30	7.7	31.9	120.1	112.0

Table 5
Measured effective mechanical properties obtained from as-built tensile coupons [36].

t_{nom} (mm)	θ (°)	E (GPa)	f_y (MPa)	f_u (MPa)	ε_u	ε_f
3	0	208	394	500	0.15	0.19
	45	211	355	469	0.12	0.15
	90	212	354	467	0.13	0.15
8	0	217	302	416	0.18	0.24
	45	192	308	427	0.15	0.19
	90	198	282	409	0.16	0.20

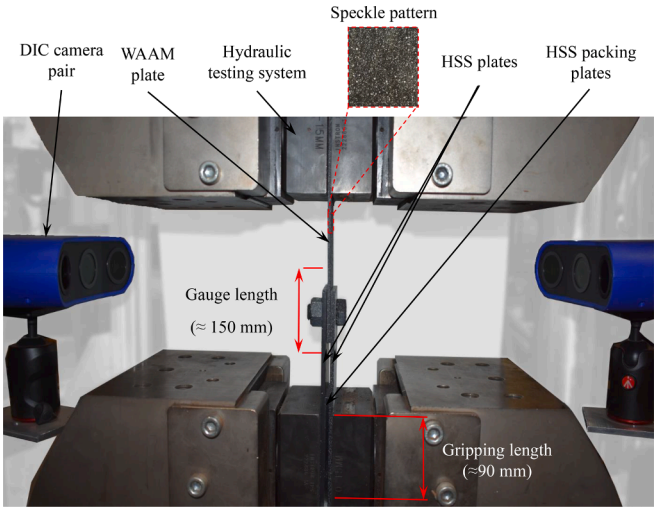

Fig. 7. Experimental setup for double-lap shear tests.

4.4. Influence of print layer orientation

The influence of print layer orientation (i.e. $\theta = 0^\circ$ or 90°) on the ultimate load capacity P_u of the WAAM specimens was not found to be significant, with the average difference in the normalised capacities between comparable specimens of different orientations being 4% – see Table 7. However, the failure modes were affected by the print layer orientations, with the $\theta = 90^\circ$ specimens mainly failing in shear-out, while the corresponding 0° specimens tended to fail in end-splitting – see Figs. 14(a) and 14(b). This difference is attributed to more severe imperfections in the transverse direction at the ends of the 0° specimens, resulting in lower resistances to end-splitting.

Furthermore, several 90° specimens (i.e. D3-85-57.2-90, D8-90-52-90 and D8-120-80-90) failed in net section tension, while most of their 0° counterparts failed in shear-out or end-splitting (i.e. D8-120-80-0 in shear-out, D8-90-52-0 and D3-85-57.2-0 in end-splitting), indicating that when shear-out and net section tension capacities are of similar magnitude, fracture lines tend to develop along the print layers – see Figs. 14(c) and 14(d).

5. Available design equations

5.1. Eurocode 3

The bearing capacity of a bolted shear connection is specified in EN 1993-1-8 [51] as:

$$P_{b,EC3} = k_m \alpha_h f_u dt \tag{1}$$

where

$$\alpha_b = min\left(\frac{e_1}{d_0}; 3\frac{f_{ub}}{f_u}; 3\right) \tag{2}$$

In Eqs. (1) and (2), k_m is equal to unity for steel grades lower than S460, e_1 is the end distance, d and d_0 are the diameters of the bolt and bolt hole respectively, f_u and f_{ub} are the tensile strengths of the plate and bolt respectively and t is the thickness of the plate. Note that for connections with a sufficiently strong bolt (i.e. $f_{ub}/f_u > 1$), according to the definition of α_b, Eurocode 3 regards the failure mode of shear-out as a special case of bearing failure, occurring when the end distance e_1 is less than 3 times the bolt hole diameter d_0.

The net section tension resistance $P_{n,EC3}$ of a bolted shear connection is defined in EN 1993-1-1 [52] as:

$$P_{n,EC3} = kA_n f_u \tag{3}$$

Table 6
Summary of experimental results.

Specimen	Test		Eurocode 3 Eqs. (1,3)		AISI S100 Eqs. (4,5,7)		AISC 360 Eqs. (8,9,10)		AS/NZS 4600 Eqs. (4,7,11)	
	P_u (kN)	FM	$\frac{P_u}{P_{EC3}}$	FM	$\frac{P_u}{P_{AISI}}$	FM	$\frac{P_u}{P_{AISC}}$	FM	$\frac{P_u}{P_{AS/NZS}}$	FM
D3-35-27-90	23.07	NS[1]	1.07	NS	1.13	NS	1.07	NS	1.13	NS
D3-35-27-0	20.83	NS	0.96	NS	1.01	NS	0.96	NS	1.01	NS
D3-45-27-90	39.13	NS	1.16	(SO)[2]	1.29	(SO)	1.04	NS	1.12	NS
D3-45-27-0	39.24	NS	1.10	(SO)	1.23	(SO)	0.98	(SO)	1.05	NS
D3-45-36-90	39.03	NS	1.02	NS	1.09	NS	1.02	NS	1.09	NS
D3-45-36-0	39.27	NS	0.98	NS	1.05	NS	0.98	NS	1.05	NS
D3-55-27-90	34.34	ES	1.14	(SO)	1.26	(SO)	1.01	(SO)	1.01	(SO)
D3-55-27-0	34.27	ES	1.10	(SO)	1.22	(SO)	0.97	(SO)	0.97	(SO)
D3-65-21.6-90	31.04	SO	1.18	SO	1.49	SO	1.19	SO	1.06	SO
D3-65-21.6-0	30.24	ES	1.11	(SO)	1.40	(SO)	1.12	(SO)	1.00	(SO)
D3-65-27-90	38.50	ES	1.17	(SO)	1.30	(SO)	1.04	(SO)	1.05	(SO)
D3-65-27-0	38.28	ES	1.08	(SO)	1.20	(SO)	0.96	(SO)	0.96	(SO)
D3-65-32.4-90	46.13	ES	1.16	(SO)	1.19	(SO)	0.95	(SO)	1.04	(SO)
D3-65-32.4-0	46.31	ES	1.08	(SO)	1.11	(SO)	0.89	(SO)	0.97	(SO)
D3-65-36-90	48.42	SO	1.14	SO	1.13	SO	0.90	SO	1.02	SO
D3-65-36-0	47.37	ES	1.04	(SO)	1.04	(SO)	0.83	(SO)	0.94	(SO)
D3-65-43.2-90	57.06	IB	1.14	(SO)	1.07	(SO)	0.94	(NS)	1.02	(SO)
D3-65-43.2-0	60.96	IB	1.10	(SO)	1.03	(SO)	0.90	(NS)	0.98	(SO)
D3-85-33-90	44.69	SO	1.15	SO	1.31	SO	1.05	SO	1.05	SO
D3-85-33-0	46.86	ES	1.11	(SO)	1.26	(SO)	1.01	(SO)	1.01	(SO)
D3-85-57.2-90	75.67	NS	1.12	(SO)	1.05	(SO)	0.98	(B)	1.02	(SO)
D3-85-57.2-0	74.42	ES	1.02	(SO)	0.96	(SO)	0.90	(B)	0.94	(SO)
D3-105-37.4-90	51.87	SO	1.15	SO	1.23	SO	0.99	SO	1.04	SO
D3-105-37.4-0	52.31	ES	1.16	(SO)	1.21	(SO)	0.97	(SO)	1.03	(SO)
D3-105-39.6-90	53.89	ES	1.15	(SO)	1.20	(SO)	0.96	(SO)	1.04	(SO)
D3-105-39.6-0	51.96	ES	1.20	(SO)	1.26	(SO)	1.01	(SO)	1.05	(SO)
D3-105-48.4-90	66.90	ES	1.19	(SO)	1.16	(SO)	0.93	(SO)	1.07	(SO)
D3-105-48.4-0	65.66	ES	1.14	(SO)	1.10	(SO)	0.88	(SO)	1.01	(SO)
D3-145-91-90	102.43	B	1.14	B	0.88	(SO)	1.14	B	0.90	(SO)
D3-145-91-0	83.56	B	0.86	B	0.67	(SO)	0.86	B	0.69	(SO)
D3-145-104-90	85.83	B	0.97	B	0.73	B	0.97	B	0.73	B
D3-145-104-0	92.86	B	0.95	B	0.71	B	0.95	B	0.71	B
D3-145-117-90	84.61	B	0.94	B	0.70	B	0.94	B	0.70	B
D3-145-117-0	92.77	B	0.96	B	0.77	(NS)	0.96	B	0.77	(NS)
D8-45-44.2-90	61.85	NS	1.09	NS	1.14	NS	1.09	NS	1.14	NS
D8-45-44.2-0	66.32	NS	1.08	NS	1.14	NS	1.08	NS	1.14	NS
D8-55-44.2-90	91.79	NS	1.06	NS	1.12	NS	1.06	NS	1.12	NS
D8-55-44.2-0	105.33	NS	1.11	NS	1.17	NS	1.11	NS	1.17	NS
D8-75-44.2-90	144.85	NS	1.18	(SO)	1.28	(SO)	1.03	(SO)	1.09	(SO)
D8-75-44.2-0	147.67	NS	1.21	(SO)	1.31	(SO)	1.05	(SO)	1.11	(SO)
D8-80-44.2-90	152.07	SO	1.25	SO	1.35	SO	1.08	SO	1.14	SO
D8-80-44.2-0	169.12	SO	1.26	SO	1.38	SO	1.10	SO	1.17	SO
D8-90-26-90	85.52	SO	1.12	SO	1.73	SO	1.38	SO	1.04	SO
D8-90-26-0	87.55	SO	1.13	SO	1.74	SO	1.39	SO	1.05	SO
D8-90-39-90	134.02	ES	1.19	(SO)	1.37	(SO)	1.10	(SO)	1.10	(SO)
D8-90-39-0	138.22	ES	1.19	(SO)	1.38	(SO)	1.10	(SO)	1.10	(SO)
D8-90-52-90	182.50	NS	1.21	(SO)	1.24	(SO)	0.99	(SO)	1.12	(SO)
D8-90-52-0	182.68	ES	1.22	(SO)	1.25	(SO)	1.00	(SO)	1.12	(SO)
D8-90-65-90	208.76	NS	1.10	(SO)	1.11	NS	1.03	NS	1.11	NS
D8-90-65-0	208.77	NS	1.11	(SO)	1.13	NS	1.04	NS	1.13	NS
D8-90-91-90	206.40	NS	1.06	NS	1.11	NS	1.03	NS	1.11	NS
D8-90-91-0	214.92	NS	1.05	NS	1.13	NS	1.05	NS	1.13	NS
D8-120-48-90	162.28	SO	1.15	SO	1.35	SO	1.08	SO	1.09	SO
D8-120-48-0	155.10	SO	1.11	SO	1.30	SO	1.04	SO	1.05	SO
D8-120-64-90	216.10	SO	1.15	SO	1.20	SO	0.96	SO	1.09	SO
D8-120-64-0	207.64	SO	1.10	SO	1.15	SO	0.92	SO	1.04	SO
D8-120-80-90	276.15	NS	1.14	(SO)	1.12	(SO)	0.98	NS	1.07	(SO)
D8-120-80-0	276.66	SO	1.18	SO	1.15	SO	1.00	(NS)	1.11	SO
D8-120-112-90	267.86	NS	1.03	NS	1.04	NS	0.97	NS	1.04	NS
D8-120-112-0	280.28	NS	1.03	NS	1.10	NS	1.02	NS	1.10	NS
Mean			1.11		1.17		1.02		1.03	
COV			0.073		0.175		0.099		0.108	

[1] SO: Shear-out, NS: net section tension, B: bearing, ES: end-splitting, IB: incidental block shear.
[2] In brackets if different from test results.

where f_u is the yield strength of the plate, A_n is the net cross-section area and k is equal to unity for plates with smooth bolt holes (i.e. fabricated by water jet cutting), as is the case for the specimens examined herein.

5.2. AISI S100

In AISI S100-16 [53], the bearing capacity $P_{b,AISI}$ of a bolted connection, for the cases where the bolt hole deformation is not a design consideration, is given by:

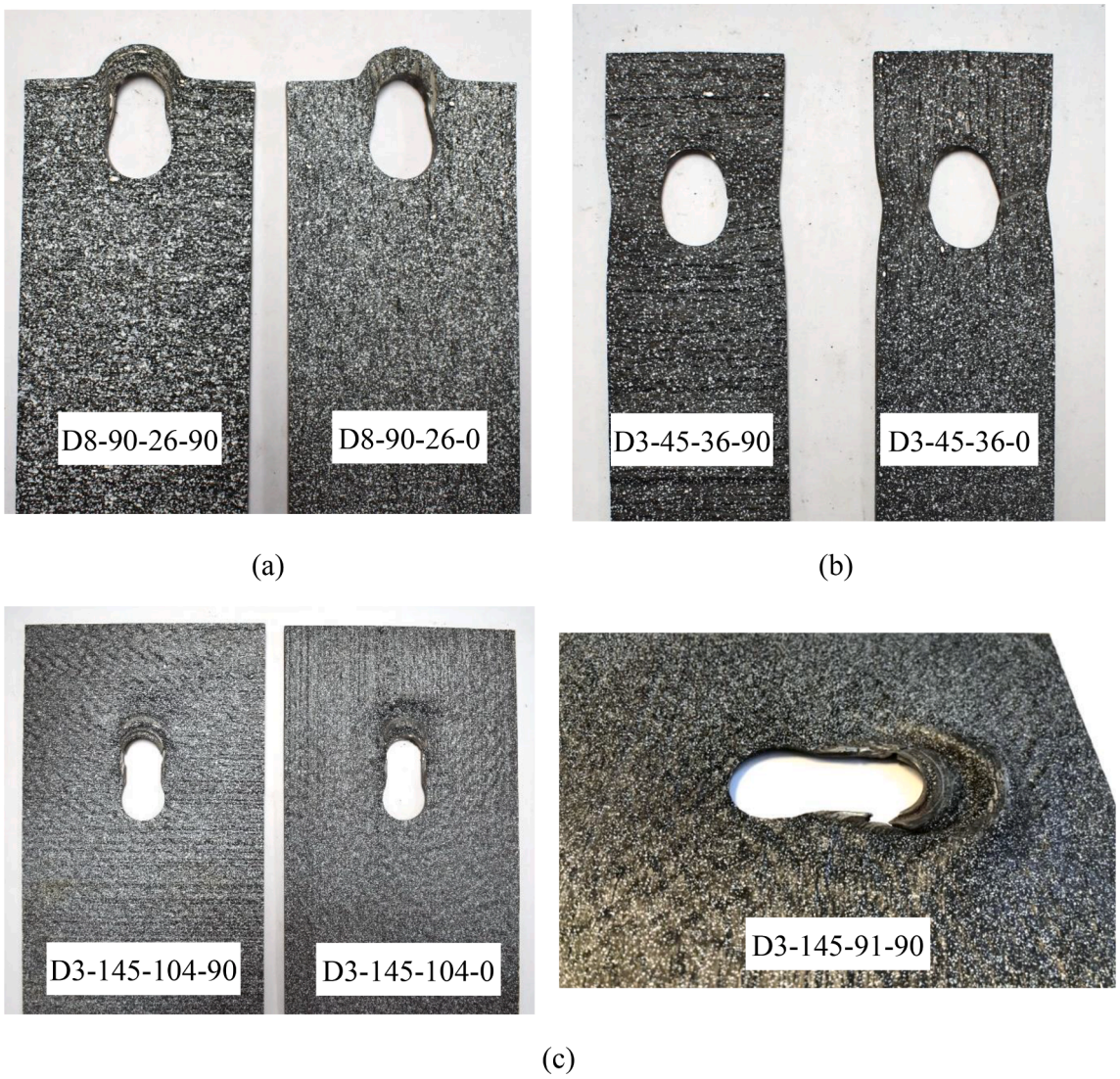

Fig. 8. Typical failure modes: (a) shear-out, (b) net section tension and (c) bearing failure.

$$P_{b,AISI} = Cm_f dtf_u \tag{4}$$

where C is a bearing factor which is equal to 3.0 when d/t is less than 10 and m_f is a modification factor, which is equal to 1.33 for the inner plates of double-shear connections.

The shear resistance $P_{s,AISI}$ is defined as:

$$P_{s,AISI} = 0.6A_{nv}f_u \tag{5}$$

in which:

$$A_{nv} = 2L_{nv}t \tag{6}$$

In Eqs. (5) and (6), A_{nv} and L_{nv} are the area and length of the net shear plane respectively, as defined in Fig. 15.

The net section tension resistance $P_{n,AISI}$ was defined in [13] and adopted by AISI S100-16 [53] as:

$$P_{n,AISI} = A_n f_u \left(0.9 + \frac{0.1d}{b}\right) \tag{7}$$

where b is the width of the plate.

5.3. AISC 360

According to AISC 360-16 [54], the bearing capacity $P_{b,AISC}$ is:

$$P_{b,AISC} = 3.0dtf_u \tag{8}$$

The shear-out capacity $P_{s,AISC}$ is defined as:

$$P_{s,AISC} = 1.5L_{nv}tf_u \tag{9}$$

while the net section tension capacity $P_{n,AISC}$ is defined as:

$$P_{n,AISC} = A_n f_u \tag{10}$$

5.4. AS/NZS 4600

Eqs. (4) and (7) are used in AS/NZS 4600 [55] to predict the bearing and the net section capacities respectively, while Eq. (11) is used to predict the shear-out capacity:

$$P_{s,AS/NZS} = L_{gv}tf_u \tag{11}$$

where L_{gv} is the length of the gross shear plane, which is equal to the end distance e_1, as per Fig. 15.

5.5. Summary of design specifications

The equations provided in the above-mentioned design standards for

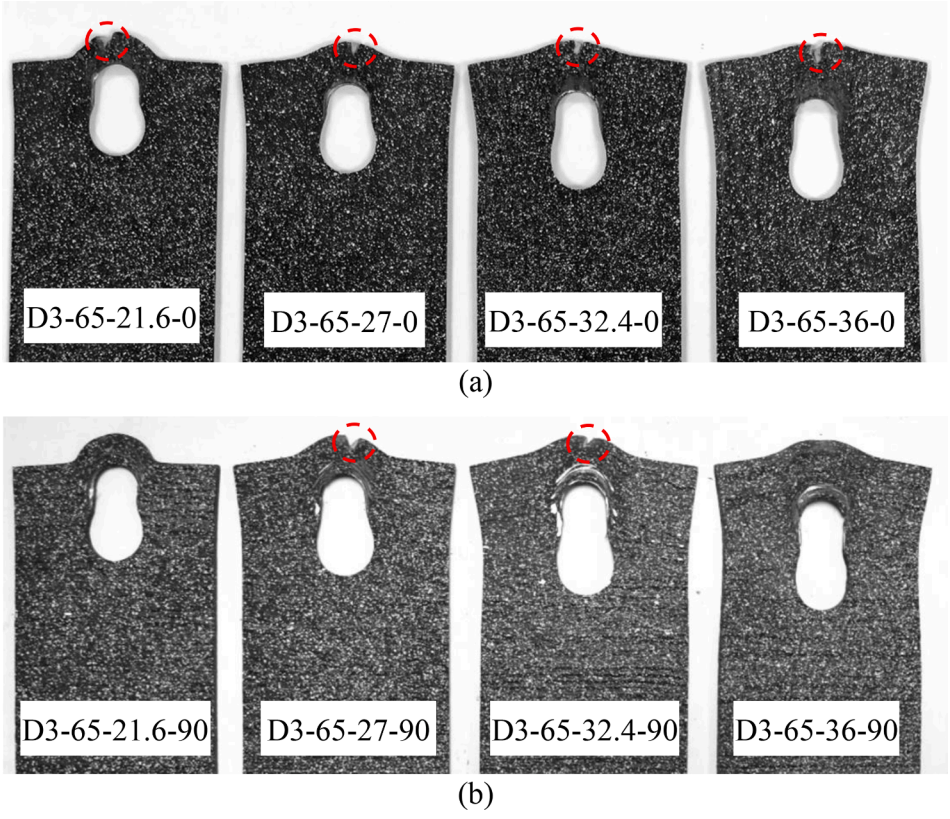

Fig. 9. Shear-out and end-splitting failures of specimens with $b = 65$ mm and (a) $\theta = 0°$ and (b) $\theta = 90°$.

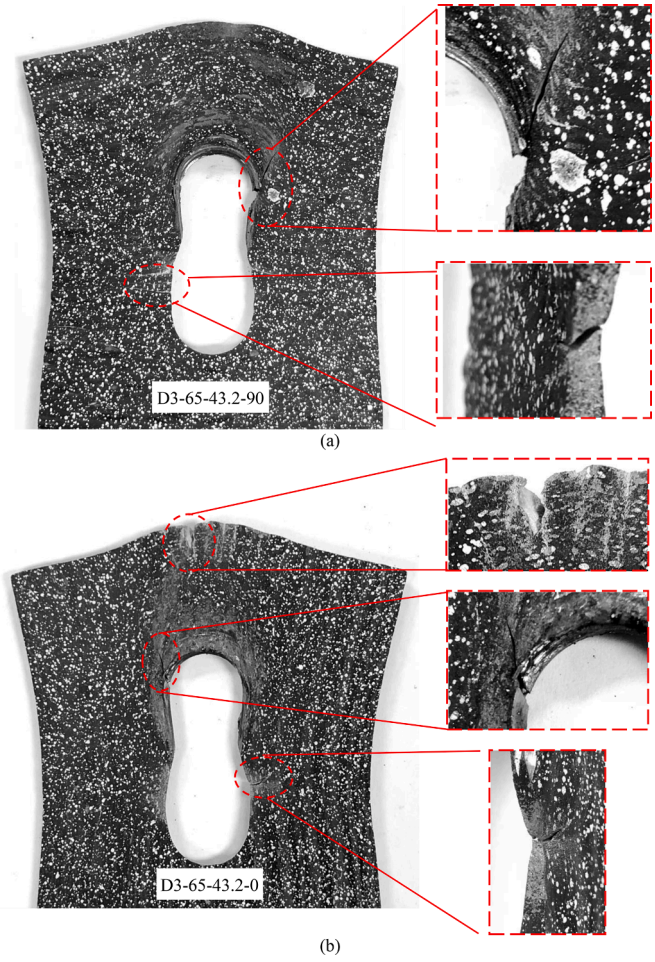

Fig. 10. Specimens failing in incidental block shear (a) Specimen D3-65-43.2-90 and (b) Specimen D3-65-43.2-0.

the different failure modes of double-lap shear connections can be summarised as follows:

$$P_b = C_b dtf_u \tag{12}$$

$$P_s = C_s A_v f_u \tag{13}$$

$$P_n = C_n A_n f_u \tag{14}$$

where the subscripts b, s and n stand for bearing, shear-out and net section failure respectively, P is the capacity prediction, C is a modification factor (C_b: bearing factor, C_s: shear factor and C_n: shear lag factor), A_v is the area of the shear plane (net, gross or active shear plane – see Fig. 15) and A_n is the area of the net section.

5.6. Proposed equations in the literature

The original form of Eq. (15) was proposed in [15] and modified in [18] for predicting the shear-out capacity in bolted connections, accounting for catenary action:

$$P_s = 1.2\left(\frac{3d}{e_1}\right)^p L_{av} t f_u \tag{15}$$

in which:

$$L_{av} = e_1 - \frac{d_0}{4} \tag{16}$$

where L_{av} is the length of the active shear plane, as illustrated in Fig. 15. Note that the effect of catenary action is considered by the catenary factor $(3d/e_1)^p$, where the power factor p can be determined empirically based on laboratory test results [18]. For the WAAM connections examined herein, p was taken as equal to 1/10.

6. Comparisons between test and predicted capacities

Comparisons between the test results and the nominal capacities and failure modes predicted by the above-mentioned design standards are presented in Table 6, where brackets are used to mark incorrect failure mode predictions. Note that the as-built material properties of the coupons with the same nominal thickness (i.e. 3 mm or 8 mm) and print layer orientation (i.e. 0° and 90°) as the tested specimens were utilised for the predictions. The bearing stress $f_b = P_u/(dt)$, normalised by the corresponding tensile stress f_u, is plotted against e_1/d in Fig. 16.

As shown in Table 6, on average the most accurate predictions are given by AISC 360 [54], with a mean test-to-predicted capacity ratio of 1.02 and a COV of 0.099. The AISC specification [54] was particularly accurate for the specimens undergoing net section tension failure (see Table 8), indicating that no in-plane shear lag factor is required for WAAM bolted connections. However, for specimens failing in shear-out, the capacity predictions were less accurate, with generally overly-conservative estimates of resistance for the specimens with short end distance (e.g. for Specimens D8-90-26-90 and D8-90-26-90, the ultimate test loads were almost 40 % greater than the predicted values) and unconservative estimates for those with relatively long end (e.g. Specimen D8-120-80-0) – see Table 9. These findings are consistent with those in the literature for conventional steel connections [15].

Among the major design specifications, Eurocode 3 [51] yielded the smallest COV value of 0.073 for all the tested specimens (see Table 6), with a reasonable mean test-to-predicted capacity ratio of 1.11. However, the code significantly underestimated the strength of specimens failing in shear-out, as evident from Table 9. For Specimens D8-80-44.2-

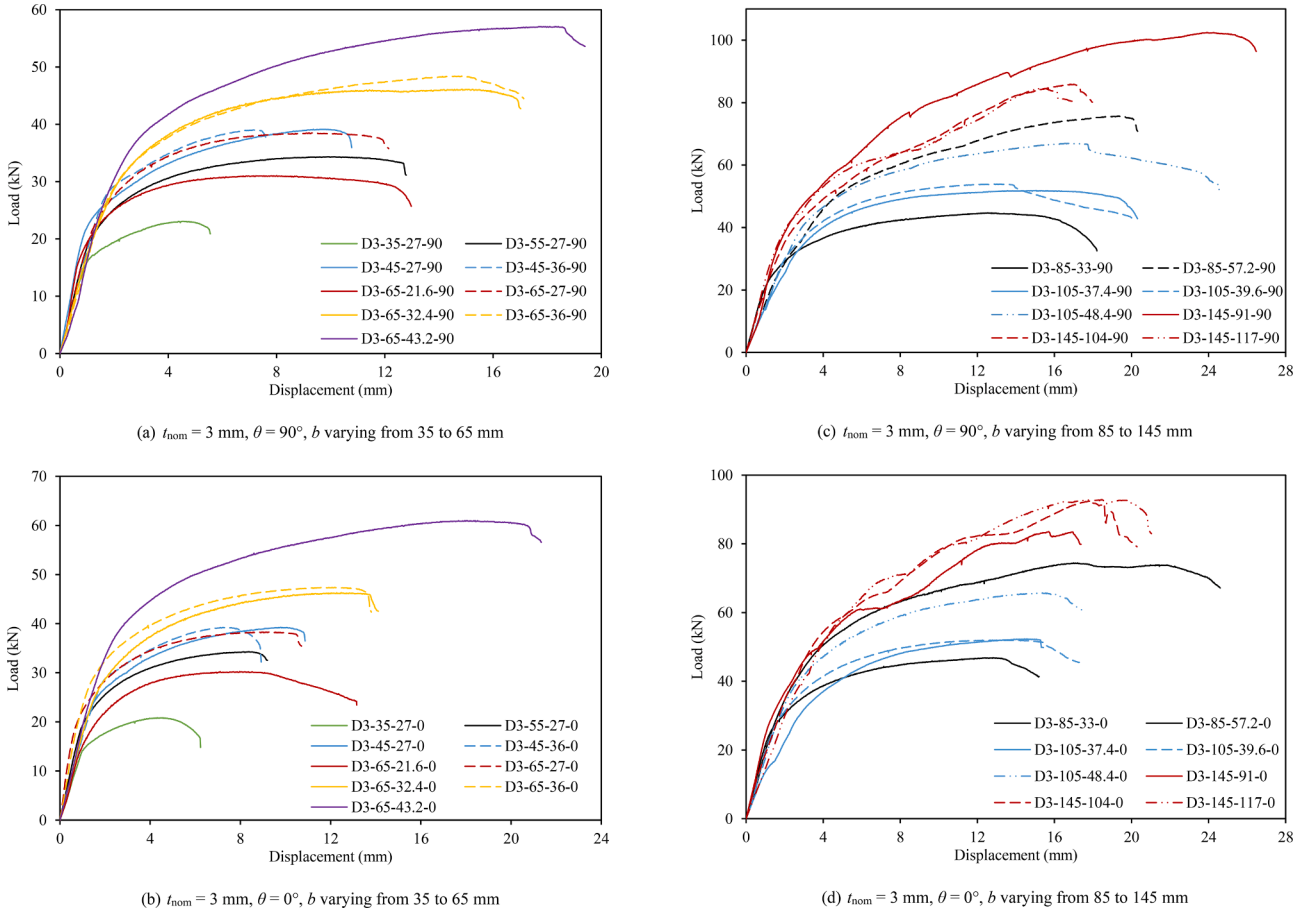

(a) t_{nom} = 3 mm, θ = 90°, b varying from 35 to 65 mm

(c) t_{nom} = 3 mm, θ = 90°, b varying from 85 to 145 mm

(b) t_{nom} = 3 mm, θ = 0°, b varying from 35 to 65 mm

(d) t_{nom} = 3 mm, θ = 0°, b varying from 85 to 145 mm

Fig. 11. Load-displacement curves of double-lap shear test specimens.

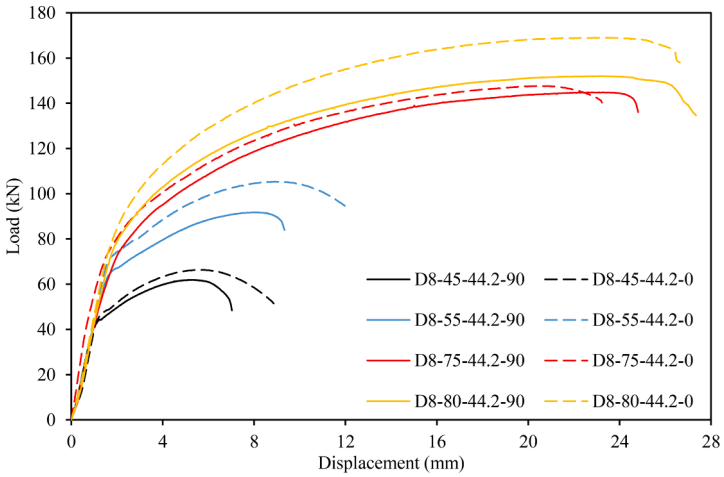

(e) t_{nom} = 8 mm, θ = 90°, 0 and b varying from 45 to 80 mm

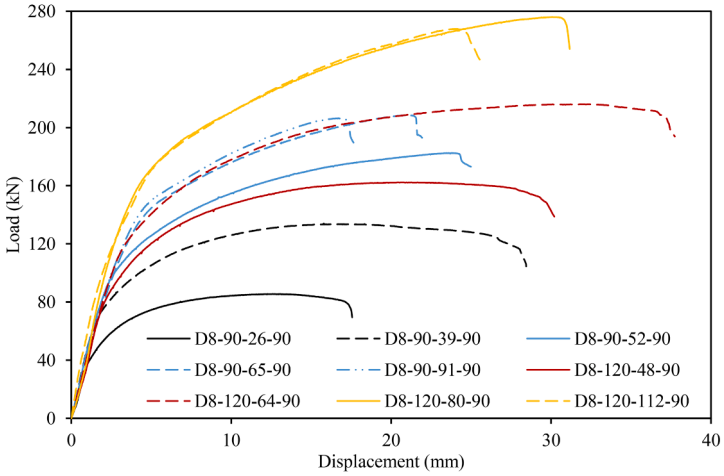

(f) t_{nom} = 8 mm, θ = 90°, b varying from 90 to 120 mm

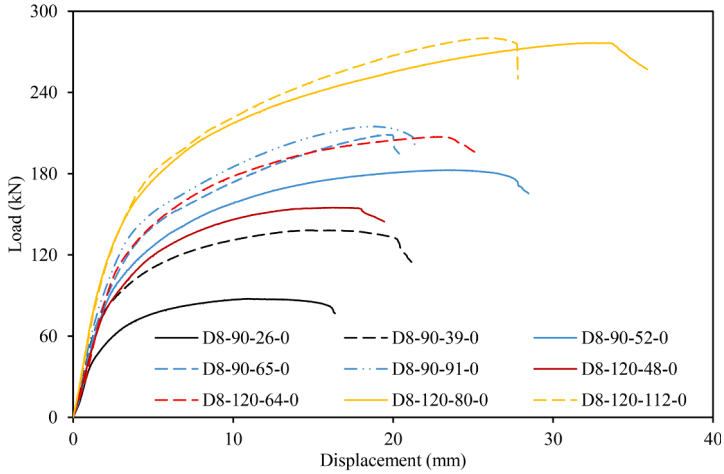

(g) t_{nom} = 8 mm, θ = 0°, b varying from 90 to 120 mm

Fig. 11. (*continued*).

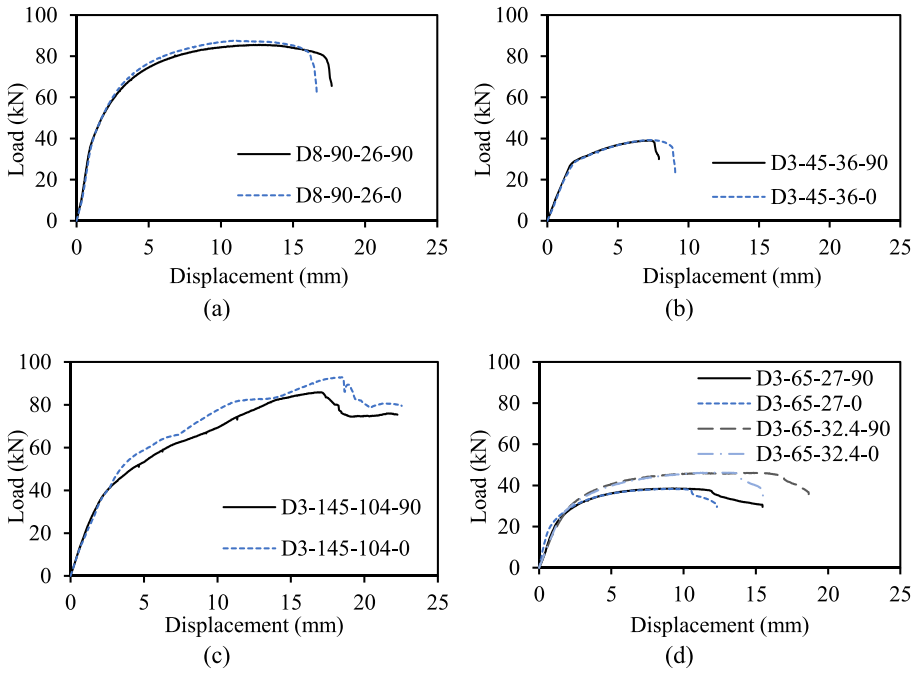

Fig. 12. Typical load-displacement curves of specimens exhibiting: (a) shear-out, (b) net section tension, (c) bearing and (d) end-splitting failure.

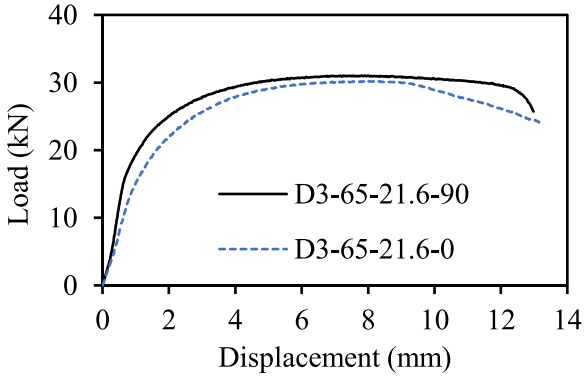

Fig. 13. Load-displacement curves of specimens failing in shear-out (D3-65-21.6-90) and end-splitting (D3-65-21.6-0).

90 and D8-80-44.2-90, the tested strengths were at least 25% higher than the predicted values. Even for the narrower Specimen D8-75-44.2-0, which actually failed in net section tension, the tested strength was over 20 % higher than the predicted shear-out strength (see Table 6).

As shown in Table 6, overall, AS/NZS 4600 [55] yielded comparable accuracy to AISC 360 [54], with a mean test-to-predicted capacity ratio of 1.03 and a COV of 0.108. However, the cold-formed steel standard [55] severely overestimated the capacities of WAAM specimens failing in bearing, by 37 % on average (see Table 10 - 1/0.73 = 1.37). The optimistic bearing resistance predictions are "offset" by the conservatism in the predictions for shear-out failure, with the bearing failure specimens D3-145-91-0 and D3-145-91-90 deemed by AS/NZS 4600 to fail in shear-out (see Tables 6 and 10).

The contrast between the optimistic predictions for bearing strengths and the conservative predictions for shear-out strengths is even more stark for the North American cold-formed steel specification AISI S100 [53]. While the specification also overestimates the bearing strength of the WAAM specimens by 37% on average as it uses the same bearing

Table 7
Influence of print layer orientation on ultimate capacity and failure mode of double-lap shear connections.

Specimen pair	$\frac{P_{u,90^\circ}}{tf_{u,90^\circ}}/\frac{P_{u,0^\circ}}{tf_{u,0^\circ}}$	FM_{90° [1]	FM_{0° [2]
D3-35-27	1.17	NS	NS
D3-45-27	1.06	NS	NS
D3-45-36	1.04	NS	NS
D3-55-27	1.04	ES	ES
D3-65-21.6	1.06	SO	ES
D3-65-27	1.09	ES	ES
D3-65-32.4	1.07	ES	ES
D3-65-36	1.11	SO	ES
D3-65-43.2	1.04	IB	IB
D3-85-33	1.03	SO	ES
D3-85-57.2	1.09	NS	ES
D3-105-37.4	0.98	SO	ES
D3-105-39.6	1.05	ES	ES
D3-105-48.4	1.06	ES	ES
D3-145-91	1.32	B	B
D3-145-104	1.02	B	B
D3-145-117	0.98	B	B
D8-45-44.2	1.00	NS	NS
D8-55-44.2	0.94	NS	NS
D8-75-44.2	0.97	NS	NS
D8-80-44.2	0.98	SO	SO
D8-90-26	1.00	SO	SO
D8-90-39	1.00	ES	ES
D8-90-52	1.00	NS	ES
D8-90-65	1.00	NS	NS
D8-90-91	0.98	NS	NS
D8-120-48	1.04	SO	SO
D8-120-64	1.04	SO	SO
D8-120-80	0.97	NS	SO
D8-120-112	0.95	NS	NS
Mean	1.04		
COV	0.072		

[1] FM_{90°: failure mode of specimens with $\theta = 90^\circ$.
[2] FM_{0°: failure mode of specimens with $\theta = 0^\circ$.

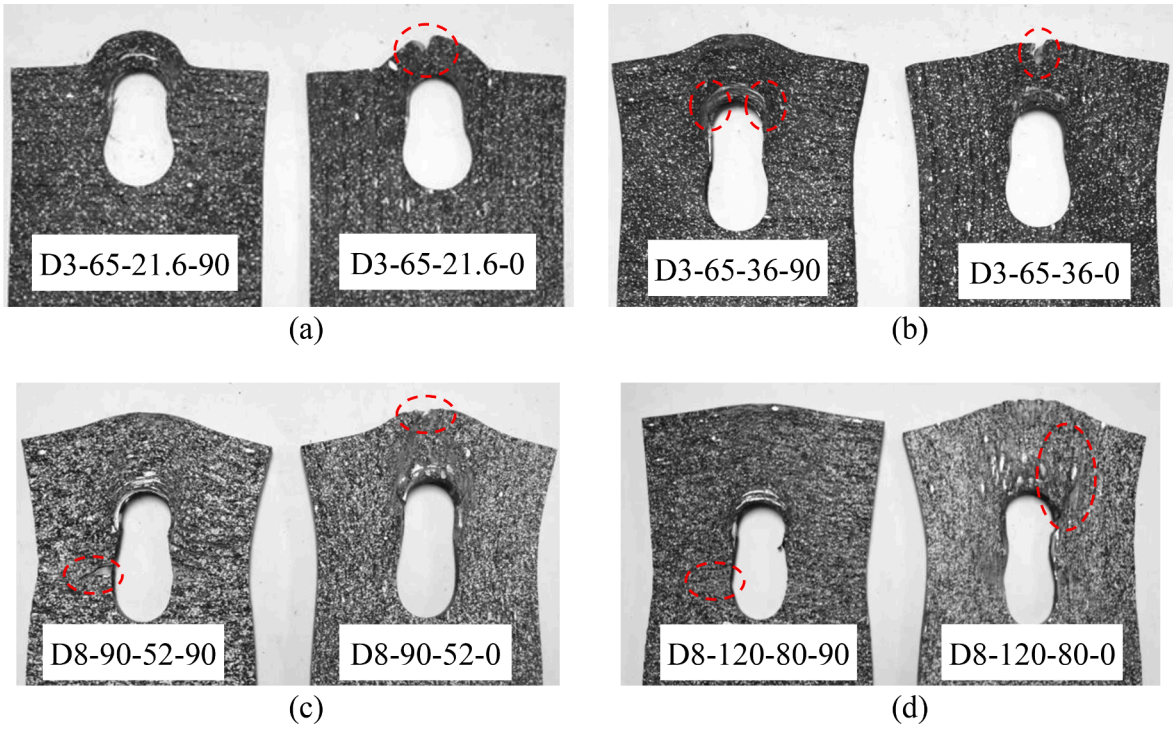

Fig. 14. Influence of print layer orientation on failure modes for different specimen pairs: (a) D3-65-21.6, (b) D3-65-36, (c) D8-90-52 and (d) D8-120-80.

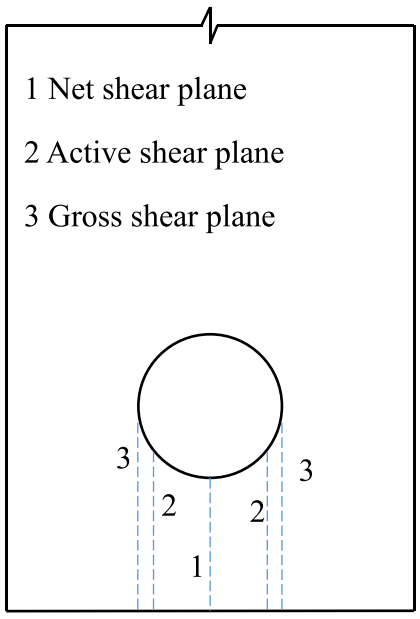

Fig. 15. Position of different shear planes [36] e_1/d.

strength equation as AS/NZS 4600 [55], the actual shear-out strengths of Specimens D8-90-26-90 and D8-90-26-90 were over 70% higher than the predicted values. As shown in Table 9, on average the actual shear-out strengths were 35% higher than the predictions of the AISI S100 specification.

While the net section tension strengths were accurately predicted by the AISC [54] and Eurocode [51] standards, with some conservatism by the AISI [53] and AS/NZS [55] standards (see Table 8), the shear-out strengths were often significantly underestimated, as evident from Table 9. In light of this, the accuracy of Eq. (15), which uses the active shear plane and accounts for catenary action [18], was also assessed, giving a mean test-to-predicted capacity ratio of 1.01 and a COV of 0.042 – see Table 9.

Although a number of test specimens failed in end-splitting, no design codes currently account for this failure mode, which is mostly predicted as shear-out failure. It is anticipated that since the shear-out capacity increases linearly with the end distance e_1 (see Fig. 16), and since the specimens failing by end-spitting were found to follow a similar trend, end-splitting capacities could be predicted using the equations for shear-out. In Table 11, comparisons between the capacities of the test specimens failing in end-splitting and predictions yielded using Eq. (15) are presented, with a mean test-to-predicted capacity ratio of 0.96 and a COV of 0.056. The best overall result is given by Eq. (11) of AS/NZS 4600 [55], with a mean test-to-predicted capacity ratio of 1.02 and a COV of 0.053.

7. Comparisons with WAAM lap connections in single shear

In this section, the findings from the present study on WAAM lap shear connections in double shear are compared to those from a previous study [36] on equivalent connections in single shear.

For the bearing capacity predictions, a notable difference between the major design specifications is that, in AISC 360 [54], no distinction is made between single and double shear connections, while in Eurocode 3 [51], AISI S100 [53] and AS/NZS 4600 [55], different values of the modification factor m_f are used to account for the two different configurations (e.g. in AISI S100, $m_f = 0.75$ for single shear and $m_f = 1.33$ for double-shear connections). In [36], WAAM lap specimens of the same dimensions as the ones examined herein but subjected to single shear were tested; their capacities P_u are compared against the capacities of the corresponding double-shear specimens in Table 12.

Since curling was restricted for the inner plates of the double-shear connections, localised tearing and curl-bearing failures [36] were eliminated from the present specimens. However, no statistically significant differences were observed between the single and the double-shear capacities except for the single shear specimens failing by curl-bearing vis-a-vis the double-shear counterparts, for which the average single-to-double shear capacity ratio was 0.63. A curl-bearing strength

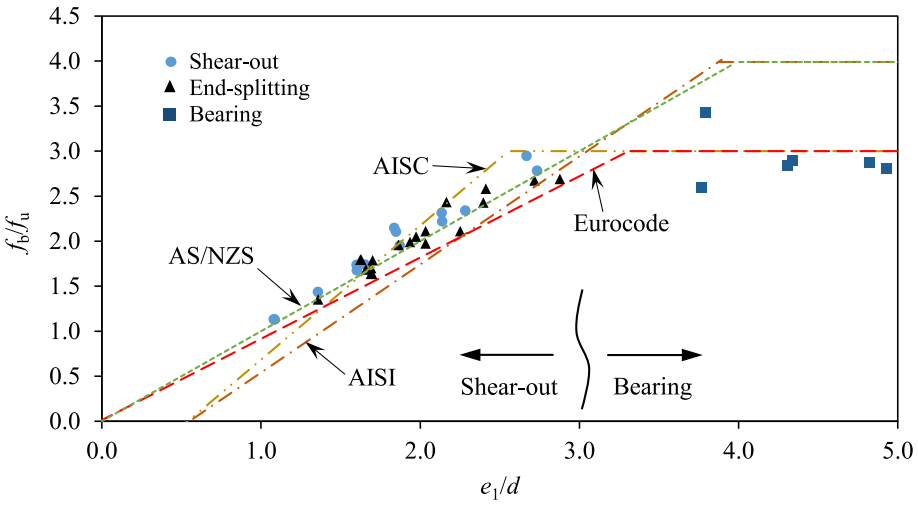

Fig. 16. Comparison of experimental results and design equations for shear-out and bearing, where shear-out and bearing failure, as described by the considered design codes, are indicated.

Table 8
Assessment of design methods for net section tension failure.

Specimen	$\frac{P_u}{P_{NS,EC3}}$	$\frac{P_u}{P_{NS,AISI}}$	$\frac{P_u}{P_{NS,AISC}}$	$\frac{P_u}{P_{NS,AS/NZS}}$
D3-35-27-90	1.07	1.13	1.07	1.13
D3-35-27-0	0.96	1.01	0.96	1.01
D3-45-27-90	1.04	1.12	1.04	1.12
D3-45-27-0	0.98	1.05	0.98	1.05
D3-45-36-90	1.02	1.09	1.02	1.09
D3-45-36-0	0.98	1.05	0.98	1.05
D3-85-57.2-90	0.92	1.00	0.92	1.00
D8-45-44.2-90	1.09	1.14	1.09	1.14
D8-45-44.2-0	1.08	1.14	1.08	1.14
D8-55-44.2-90	1.06	1.12	1.06	1.12
D8-55-44.2-0	1.11	1.17	1.11	1.17
D8-75-44.2-90	0.98	1.05	0.98	1.05
D8-75-44.2-0	1.02	1.09	1.02	1.09
D8-90-52-90	0.91	0.99	0.91	0.99
D8-90-65-90	1.03	1.11	1.03	1.11
D8-90-65-0	1.04	1.13	1.04	1.13
D8-90-91-90	1.03	1.11	1.03	1.11
D8-90-91-0	1.05	1.13	1.05	1.13
D8-120-80-90	0.98	1.06	0.98	1.06
D8-120-112-90	0.97	1.04	0.97	1.04
D8-120-112-0	1.02	1.10	1.02	1.10
Mean	1.02	1.09	1.02	1.09
COV	0.052	0.047	0.052	0.047

Table 9
Assessment of design methods for shear-out failure.

Specimen	$\frac{P_u}{P_{SO,EC3}}$	$\frac{P_u}{P_{SO,AISI}}$	$\frac{P_u}{P_{SO,AISC}}$	$\frac{P_u}{P_{SO,AS/NZS}}$	$\frac{P_u}{P_{SO,Teh}}$
D3-65-21.6-90	1.18	1.49	1.19	1.06	1.02
D3-65-36-90	1.14	1.13	0.90	1.02	0.95
D3-85-33-90	1.15	1.31	1.05	1.05	0.99
D3-105-37.4-90	1.15	1.23	0.99	1.04	0.97
D8-80-44.2-90	1.25	1.35	1.08	1.14	1.06
D8-80-44.2-0	1.26	1.38	1.10	1.17	1.09
D8-90-26-90	1.12	1.73	1.38	1.04	1.04
D8-90-26-0	1.13	1.74	1.39	1.05	1.05
D8-120-48-90	1.15	1.35	1.08	1.09	1.02
D8-120-48-0	1.11	1.30	1.04	1.05	0.98
D8-120-64-90	1.15	1.20	0.96	1.09	1.00
D8-120-64-0	1.10	1.15	0.92	1.04	0.95
D8-120-80-0	1.18	1.15	0.92	1.11	1.01
Mean	1.16	1.35	1.08	1.07	1.01
COV	0.042	0.149	0.149	0.041	0.042

Table 10
Assessment of design methods for bearing failure.

Specimen	$\frac{P_u}{P_{B,EC3}}$	$\frac{P_u}{P_{B,AISI}}$	$\frac{P_u}{P_{B,AISC}}$	$\frac{P_u}{P_{B,AS/NZS}}$
D3-145-91-90	1.14	0.86	1.14	0.86
D3-145-91-0	0.86	0.65	0.86	0.65
D3-145-104-90	0.97	0.73	0.97	0.73
D3-145-104-0	0.95	0.71	0.95	0.71
D3-145-117-90	0.94	0.70	0.94	0.70
D3-145-117-0	0.96	0.72	0.96	0.72
Mean	0.97	0.73	0.97	0.73
COV	0.095	0.096	0.095	0.096

Table 11
Assessment of design methods for end-splitting failure using shear-out equations.

Specimen	$\frac{P_u}{P_{SO,EC3}}$	$\frac{P_u}{P_{SO,AISI}}$	$\frac{P_u}{P_{SO,AISC}}$	$\frac{P_u}{P_{SO,AS/NZS}}$	$\frac{P_u}{P_{SO,Teh}}$
D3-55-27-90	1.14	1.26	1.01	1.01	0.95
D3-55-27-0	1.10	1.22	0.97	0.97	0.92
D3-65-21.6-0	1.11	1.40	1.12	1.00	0.96
D3-65-27-90	1.17	1.30	1.04	1.05	0.99
D3-65-27-0	1.08	1.20	0.96	0.96	0.91
D3-65-32.4-90	1.16	1.19	0.95	1.04	0.96
D3-65-32.4-0	1.08	1.11	0.89	0.97	0.90
D3-65-36-0	1.04	1.04	0.83	0.94	0.87
D3-85-33-0	1.11	1.26	1.01	1.01	0.95
D3-85-57.2-0	1.02	0.96	0.77	0.94	0.86
D3-105-37.4-0	1.16	1.21	0.97	1.03	0.96
D3-105-39.6-90	1.15	1.20	0.96	1.04	0.97
D3-105-39.6-0	1.20	1.26	1.01	1.05	0.99
D3-105-48.4-90	1.19	1.16	0.93	1.07	0.99
D3-105-48.4-0	1.14	1.10	0.88	1.01	0.94
D8-90-39-90	1.19	1.37	1.10	1.10	1.04
D8-90-39-0	1.19	1.38	1.10	1.10	1.04
D8-90-52-0	1.22	1.25	1.00	1.12	1.04
Mean	1.14	1.22	0.97	1.02	0.96
COV	0.050	0.094	0.094	0.053	0.056

Table 12
Comparisons between the single and double shear capacities.

Single shear lap tests			Double shear lap tests		$\frac{P_{u,S}}{t_S}/\frac{P_{u,D}}{t_D}$ [1]
Specimen	FM		Specimen	FM	
S3-55-27-90	LT		D3-55-27-90	ES	1.08
S3-55-27-0	LT		D3-55-27-0	ES	1.13
S3-45-27-90	NS/LT		D3-45-27-90	NS	0.91
S3-45-27-0	NS/LT		D3-45-27-0	NS	0.93
S3-45-36-90	NS/LT		D3-45-36-90	NS	0.93
S3-45-36-0	NS/LT		D3-45-36-0	NS	0.91
S3-35-27-90	NS		D3-35-27-90	NS	0.93
S3-35-27-0	NS		D3-35-27-0	NS	1.04
S3-65-21.6-90	SO		D3-65-21.6-90	SO	1.00
S3-65-21.6-0	SO		D3-65-21.6-0	ES	1.01
S3-65-27-90	LT		D3-65-27-90	ES	1.14
S3-65-27-0	SO		D3-65-27-0	ES	1.11
S3-65-32.4-90	LT		D3-65-32.4-90	ES	0.96
S3-65-32.4-0	LT		D3-65-32.4-0	ES	0.98
S3-65-36-90	LT		D3-65-36-90	SO	0.84
S3-65-36-0	LT		D3-65-36-0	ES	0.90
S3-85-33-90	LT		D3-85-33-90	SO	0.96
S3-85-33-0	LT		D3-85-33-0	ES	1.05
S3-105-39.6-90	LT		D3-105-39.6-90	ES	0.98
S3-105-39.6-0	LT		D3-105-39.6-0	ES	0.94
		Mean			0.99
		COV			0.083
S3-145-104-90	CB		D3-145-104-90	B	0.64
S3-145-104-0	CB		D3-145-104-0	B	0.61
		Mean			0.63
		COV			0.036

[1] $P_{u,S}$: ultimate load of single shear tests; $P_{u,D}$: ultimate load of double shear tests; t_S: measured thickness in single shear tests; t_D: measured thickness in double shear tests.

equation has been proposed for single-shear bolted connections [36].

8. Conclusions

Sixty tests on WAAM steel double-lap shear bolted connections of two nominal thicknesses and print layer orientations were carried out, proportioned to trigger different failure modes such as shear-out, net section tension, bearing and end-splitting. The material properties, load-deformation responses and observed failure modes were presented and analysed. The print layer orientation was found to have an insignificant effect on the ultimate capacities of the examined double-lap specimens, consistent with an earlier finding for single-lap specimens [36]. However, the specimens with print layers parallel to the loading direction were more likely to fail by end-splitting.

The test results were used to evaluate the applicability of equations currently used for conventional steel lap connections in design standards, namely Eurocode 3 [51] and AISC 360 [54] for structural steel and AISI S100 [53] and AS/NZS 4600 [55] for cold-formed steel. The net section tension and bearing failure capacity predictions obtained using the structural steel specifications [51,54] were more accurate than those determined using the cold-formed steel specifications [53,55] (by 7% and 24% respectively).

Shear-out strengths were often overestimated by all specifications. Depending on the end distance, the tested shear-out strengths were higher than the specifications' estimates by up to 26%, 73%, 39% and 17% for Eurocode 3 [51], AISI S100 [53], AISC 360 [54] and AS/NZS 4600 [55], respectively. The shear-out strengths were accurately predicted using an equation found in the literature [18], which makes use of the active shear plane in conjunction with the catenary effect.

Interestingly, the end-splitting failure loads could be predicted accurately using the shear-out equation of AS/NZS 4600 [55], where the end distance is measured from the centre of the bolt hole. This outcome indicates that the active shear plane has no role in determining the end-splitting strength.

Overall, the structural steel specifications [51,54] were found to provide more accurate predictions than the cold-formed steel specifications [53,55]; this may relate to the ductility of the WAAM steel material being closer to that of the structural (hot-rolled) steel than cold-formed steel. However, the accuracy of the specifications can be improved further based on the results presented in this paper. This will be addressed in future research. Note that the uncertainty of the failure mode prediction is also attributed to the geometrical irregularity of the WAAM specimens, owing to the surface undulations inherent to the WAAM process. The extent to which this can be mitigated by controlling and monitoring the printing parameters during WAAM will also be explored in future work.

CRediT authorship contribution statement

Xi Guo: Writing – review & editing, Writing – original draft, Visualization, Validation, Software, Methodology, Investigation, Formal analysis, Data curation. **Pinelopi Kyvelou:** Writing – review & editing, Visualization, Validation, Supervision, Software, Methodology, Investigation, Data curation, Conceptualization. **Jun Ye:** Writing – review & editing, Software, Methodology, Investigation, Conceptualization. **Lip H. Teh:** Writing – review & editing, Validation, Supervision, Methodology, Investigation. **Leroy Gardner:** Writing – review & editing, Validation, Supervision, Resources, Project administration, Methodology, Investigation, Funding acquisition, Conceptualization.

Declaration of Competing Interest

The authors declare that they have no known competing financial interests or personal relationships that could have appeared to influence the work reported in this paper.

Data availability

Data will be made available on request.

Acknowledgements

This research was possible thanks to funding and support from the European Union's Horizon 2020 research and innovation programme under grant agreement No. 820776 'Intelligent data-driven pipeline for the manufacturing of certified metal parts through Direct Energy Deposition process INTEGRADDE'. The authors also would like to acknowledge the contribution of MX3D for the fabrication of the test specimens and Gordon Herbert and Harry Slack at Imperial College London for their assistance in the programme.

References

[1] Gardner L, Kyvelou P, Herbert G, Buchanan C. Testing and initial verification of the world's first metal 3D printed bridge. J Construct Steel Res 2020;172:106233.
[2] Laghi V, Palermo M, Tonelli L, Gasparini G, Ceschini L, Trombetti T. Tensile properties and microstructural features of 304L austenitic stainless steel produced by wire and arc additive manufacturing. Int J Adv Manuf Technol 2020;106:3693–705.
[3] Silvestru VA, Ariza I, Vienne J, Michel L, Aguilar Sanchez AM, Angst U, et al. Performance under tensile loading of point-by-point wire and arc additively manufactured steel bars for structural components. Mater Des 2021;205:109740.
[4] Martina F, Mehnen J, Williams SW, Colegrove P, Wang F. Investigation of the benefits of plasma deposition for the additive layer manufacture of Ti–6Al–4V. J Mater Process Tech 2012;212(6):1377–86.
[5] Gardner L. Metal additive manufacturing in structural engineering – review, advances, opportunities and outlook. Struct 2023;47:2178–93.
[6] Kanyilmaz A, Demir AG, Chierici M, Berto F, Gardner L, Kandukuri SY, et al. Role of metal 3D printing to increase quality and resource-efficiency in the construction sector. Addit Manuf 2022;50:102541.
[7] Ye J, Kyvelou P, Gilardi F, Lu H, Gilbert M, Gardner L. An end-to-end framework for the additive manufacture of optimized tubular structures. IEEE Access 2021;9:165476–89.
[8] Rogers CA, Hancock GJ. Bolted connection tests of thin G550 and G300 sheet steels. J Struct Eng 1998;125(2):128–36.

[9] Kim HJ, Yura JA. The effect of ultimate-to-yield ratio on the bearing strength of bolted connections. J Construct Steel Res 1999;49:255–69.
[10] Aalberge A, Larsen PK. Bearing strength of bolted connections in high strength steel. In: 9th Nordic steel Construct. Conf. (2001) 859–66.
[11] Aalberge A, Larsen PK. The effect of steel strength and ductility on bearing failure of bolted connections. In: 3rd European Conf. on steel struct. (2002) 869–78.
[12] Može P, Beg D. High strength steel tension splices with one or two bolts. J Construct Steel Res 2010;66:1000–10.
[13] Teh LH, Gilbert BP. Net Section Tension Capacity of Bolted Connections in Cold-Reduced Steel Sheets. J Struct Eng 2012;138(3):337–44.
[14] Lim JS, Kim TS, Kim SH. Ultimate strength of single shear bolted connections with cold-formed ferritic stainless steel. J Zhejiang Univ Sci A (Appl Phys & Eng) 2013; 14(2):120–36.
[15] Teh LH, Uz ME. Ultimate Shear-Out Capacities of Structural-Steel Bolted Connections. J Struct Eng 2015;141(6):04014152.
[16] Wang Y, Lyu Y, Li G. Experimental investigation of two-bolt connections for high strength steel members. In: 12th Int. Conf. on Advances in Steel-Concrete Composite (2018) 595–600.
[17] Wang Y, Lyu Y, Li G, Liew JYR. Behavior of single bolt bearing on high strength steel plate. J Constr Steel Res 2017;137:19–30.
[18] Xing H, Teh LH, Jiang Z, Ahmed A. Shear-Out Capacity of Bolted Connections in Cold-Reduced Steel Sheets. J Struct Eng 2020;146(4):04020018.
[19] Cho Y, Teh LH, Young B. Effects of material ductility and cooling methods on the bearing strength of steel bolted connections. J Struct Eng 2021;181:106625.
[20] Rogers CA, Hancock GJ. Bolted connection design for sheet steels less than 1.0 mm thick. J Constr Steel Res 1999;51(2):123–46.
[21] Može P. Bearing strength at bolt holes in connections with large end distance and bolt pitch. J Construct Steel Res 2018;147:132–44.
[22] Cai Y, Young B. Effects of end distance on thin sheet steel bolted connections. Eng Struct 2019;196:109331.
[23] Ding C, Torabian S, Schafer BW. Strength of bolted lap joints in steel sheets with small end distance. J Struct Eng 2020;146(12):04020270.
[24] Lin XM, Yam MCH, Chung KF, Lam ACC. A study of net-section resistance of high strength steel bolted connections. Thin-Walled Struct 2021;159:107284.
[25] Jiang K, Zhao O, Tan KH. Experimental and numerical study of S700 high strength steel double shear bolted connections in tension. Eng Struct 2020;225(15):111175.
[26] Guo H, Xie Y, Liu Y, Yang D. Study on mechanical behavior of Q690D high strength steel bearing-type bolted connections. Structures 2020;23:588–601.
[27] Kim TS, Hong SK, Hwang BK, Kim JS. Block shear capacity in cold-formed lean duplex stainless steel double-shear bolted connections. Thin-Walled Struct 2021; 161:107520.
[28] Dobrić J, Cai Y, Young B, Rossi B. Behaviour of duplex stainless steel bolted connections. Thin-Walled Struct 2021;169:108380.
[29] Jiang K, Zhao O, Gardner L. Block tearing of S700 high strength steel bolted connections: Testing, numerical modelling and design. Eng Struct 2021;246: 112979.
[30] Yu WW, Mosby RL. Bolted connections in cold-formed steel structures, Final report. Rolla: Univ. of Missouri-Rolla; 1981.
[31] Teh LH, Uz ME. Effect of loading direction on the bearing capacity of cold-reduced steel sheets. J struct Eng 2014;140(12):06014005.
[32] Rex CO, Easterling WS. Behavior and Modeling of a Bolt Bearing on a Single Plate. J Struct Eng 2003;129(6):792–800.
[33] Winter G. Tests on bolted connections in light gage steel. J Struct Div 1956;82(2): 1–25.
[34] Rogers CA, Hancock GJ. Failure modes of bolted-sheet-steel connections loaded in shear. J Struct Eng 2000;126(3):288–96.
[35] Teh LH, Uz ME. Ultimate Tilt-Bearing Capacity of Bolted Connections in Cold-Reduced Steel Sheets. J Struct Eng 2017;143(4):04016206.
[36] Guo X, Kyvelou P, Ye J, Teh LH, Gardner L. Testing and analysis of wire arc additively manufactured steel single-lap shear bolted connections. Thin-Walled Struct 2022;181:110029.
[37] MX3D, About – MX3D, [online] Available from https://mx3d.com, accessed Mar. 15, 2021.
[38] EN ISO 14341: 2010 Welding consumables – Wire electrodes and weld deposits for gas shielded metal arc welding of non alloy and fine grain steels- Classification, International Organization for Standardization.
[39] Faro Design ScanArm 2.0 ®, 2018.
[40] D Systems, Geomagic Wrap 2017 (Version 2017.0.2:64) [Software] 2017 D Systems, Incorporated and its licensors, 2017.
[41] Hadjipantelis N, Weber B, Buchanan C, Gardner L. Description of anisotropic material response of wire and arc additively manufactured thin-walled stainless steel elements. Thin-Walled Struct 2022;171:108634.
[42] Kyvelou P, Huang C, Gardner L, Buchanan C. Structural testing and design of wire arc additively manufactured square hollow sections. J Struct Eng 2021;147:1–19.
[43] Kyvelou P, Slack H, Mountanou DD, Wadee MA, Britton TB, Buchanan C, et al. Mechanical and microstructural testing of wire and arc additively manufactured sheet material. Mater Des 2020;192:108675.
[44] Rhino 3D, Rhino 3D computer-aided design software (Version 5 SR14 64-bit) [Software] Robert McNeel & Associates, 2017.
[45] EN ISO 6892-1: 2019 Metallic materials – tensile testing, part 1: Method of test at room temperature, International Organization for Standardization.
[46] Huang C, Kyvelou P, Zhang R, Britton TB, Gardner L. Mechanical testing and microstructural analysis of wire arc additively manufactured steels. Mater Des 2022;216:110544.
[47] Salih EL, Gardner L, Nethercot DA. Bearing failure in stainless steel bolted connections. Eng Struct 2011;33:549–62.
[48] Owens GW, Dowling PJ, Algar RJ. Bearing stresses in connections using grade 8.8 bolts, unpublished test report. Imperial College London; 1976.
[49] Može P, Beg D. A complete study of bearing stress in single bolt connections. J Construct Steel Res 2014;95:126–40.
[50] Može P. Statistical evaluation of bearing resistance and related strength functionsfor bolted connections. J Construct Steel Res 2020;171:106128.
[51] Eurocode 3: design of steel structures – part 1-8: design of joints, prEN 1993-1-8, Brussels, European Committee for Standardisation, 2021.
[52] Eurocode 3: design of steel structures – part 1-1: general rules and rules for builidng, prEN 1993-1-1, Brussels, European Committee for Standardisation, 2020.
[53] AISI S100,. North American specification for the design of cold-formed steel structural members, AISI S100–16w/S1-18. Washington DC: American Iron and Steel Institue; 2016.
[54] AISC 360, Specification for structural steel buildings, ANSI/AISC 360-16, Chicago, American Institute of Steel Construction, 2016.
[55] AS/NZS 4600, Cold-formed steel structures, AS/NZS 4600:2018, Sydney, Australian/New Zealand Standard, 2018.